Controlling photoexcited electron spin by light polarization in ultrafast-pumped altermagnets

Amir Eskandari-asl [1], Jorge I. Facio [2,3], Oleg Janson [4], Adolfo Avella [1,5,6,*] and Jeroen van den Brink [4,7,†]

[1] *Dipartimento di Fisica E.R. Caianiello, Università degli Studi di Salerno, I-84084 Fisciano (SA), Italy*

[2] *Centro Atomico Bariloche and Instituto Balseiro, CNEA, 8400 Bariloche, Argentina*

[3] *Instituto de Nanociencia y Nanotecnologia CNEA-CONICET, 8400 Bariloche, Argentina*

[4] *Leibniz Institute for Solid State and Materials Research, IFW Dresden, Helmholtzstraße 20, 01069 Dresden, Germany*

[5] *CNR-SPIN, Unità di Salerno, I-84084 Fisciano (SA), Italy*

[6] *CNISM, Unità di Salerno, Università degli Studi di Salerno, I-84084 Fisciano (SA), Italy*

[7] *Würzburg-Dresden Cluster of Excellence ct.qmat, Technische Universität Dresden, 01062 Dresden, Germany*

(Received 7 March 2025; revised 15 May 2025; accepted 28 May 2025; published 1 July 2025)

Altermagnets (AMs) constitute a novel class of spin-compensated materials in which the symmetry connecting opposite-spin sublattices involves a spatial rotation. Here, we uncover a set of unique nonlinear, light-driven properties that set AMs apart from traditional ferro- and antiferromagnets. We demonstrate theoretically that the *polarization* of an electromagnetic pulse that photo-excites electrons and holes in an AM, controls the *spin orientation* of these nonequilibrium charge carriers. For a d-wave AM model and a prototype material, a RuO_2 bilayer, we show that very large post-pump spin polarizations may be attained by exploiting resonances. We show that this protocol also allows, in an AM, to directly probe the spin splitting of the electronic states in energy and momentum space. Thus, it can be used to identify and characterize altermagnetic materials via ultrafast pump-probe Kerr/Faraday spectroscopy or spin- and time-resolved ARPES. This opens up the possibility of devising ultrafast optical switches of nonequilibrium spin-polarization, finely tunable by adjusting the pump-pulse characteristics.

DOI: 10.1103/yjp4-gkj9

I. INTRODUCTION

Altermagnetism has recently emerged as a new type of magnetic ordering, distinct from ferro- and antiferromagnetism. Similarly to antiferromagnets (AFMs), the net magnetization of altermagnets (AMs) vanishes by symmetry. They differ from AFMs because the enforcing symmetry that connects the two magnetic sublattices is not merely an inversion or translation, but also involves a rotation [1,2]. This leads to a breaking of the spin degeneracy of the electronic states in their nonrelativistic band structure with an energy scale set by the local exchange field, which is generally much larger than the relativistic spin-orbit-coupling energy scale. A large number of AMs have already been identified [3–7], and this number continues to grow. Various linear response properties of AMs have been recognized that may render them of practical interest, for instance, as spin current generators relevant for spintronics [1,2]. Also, the recently developed Landau theory of altermagnetism [8] allows to relate the formation of altermagnetic order directly to other key linear response properties such as anomalous Hall conductivity [1,9], Edelstein response [10,11] and piezomagnetic [12–14], magneto-optic, and magneto-elastic [15] effects. In particular, the linear magneto-optical response in the presence of an external magnetic field, which involves momentum- and spin-dependent matrix elements, is sensitive to the presence of altermagnetism and depends on the orientation of the ground state Néel vector [16].

Here, we take a step beyond the linear responses of AMs and consider their nonlinear, light-driven properties. In general, the possibility of controlling the physical properties of solids with ultrafast electromagnetic (EM) pulses is a fascinating goal at the core of a broad research field [17–23]. Here we set out to determine how the features of a strong time-dependent EM pulse (its polarization, frequency, amplitude, and duration) affect the properties of the pump-induced charge carriers (their density, spin, and momentum) in AMs. This is a profoundly nonlinear optical process, which involves the time evolution of the entire system and we keep track of its complete response to the pump pulse. Using the Dynamical Projective Operatorial Approach (DPOA) [23–25], which allows to efficiently study out-of-equilibrium systems by projecting the time-dependent operators on their equilibrium counterparts, we analyze the field-induced charge carriers in a d-wave AM model as well as a metallic RuO_2 bilayer, employing its electronic properties we calculated *ab initio*.

Our analysis reveals that by changing the linear polarization of the EM pump pulse, it is possible to photo-excite electrons with a specific spin orientation, exploiting the resonance of specific momentum regions of the band dispersion to the pulse frequency and, in particular, the polarization and

*Contact author: a.avella@unisa.it

†Contact author: j.van.den.brink@ifw-dresden.de

momentum dependence of the light-matter coupling per spin direction in AMs. We show how the effect can be tuned and optimized adapting the pulse characteristics and demonstrate how the large electronic spin-splittings of AMs in momentum space can be leveraged to generate large densities of pump-induced spin polarization. The pulse polarization control of the spin direction and net magnetization of photo-pumped charge carriers are underlain by the altermagnetic symmetry and thus absent in conventional ferro- or antiferromagnets.

The essential ingredient in AMs that allows photo-exciting electrons with a specific spin orientation is the anisotropy of the electronic structure of a single spin species. Without spin-orbit coupling, the Hamiltonian is block diagonal with respect to the two spin species, σ and $-\sigma$, so that the symmetry of each spin-block can be considered separately. For instance, in a two-dimensional d-wave AM, the electronic structure of the spin-species σ has a twofold rotation *symmetry*, C_2, which implies in general the presence of an optical anisotropy along the two orthogonal axes $\boldsymbol{a}$ and $\boldsymbol{b}$ of the lattice. For a given excitation frequency and linear photon polarization of the impinging electric field, $\boldsymbol{E}$, *in extrema*, an optical transition could be allowed along one axis (let us say, $\boldsymbol{E} \parallel \boldsymbol{a}$) and forbidden along the other one ($\boldsymbol{E} \parallel \boldsymbol{b}$), for the spin species σ under consideration. The d-wave AM has a lattice symmetry and magnetic ordering such that it restores a fourfold rotation symmetry (which in principle renders $\boldsymbol{a}$ and $\boldsymbol{b}$ equivalent), but only when it is combined with time reversal, which maps σ to $-\sigma$. Having this C_4T *symmetry* in the electronic structure implies that the excitation cross section of σ with photon polarization along $\boldsymbol{a}$, is equal to that of $-\sigma$ with photon polarization along $\boldsymbol{b}$. In the extreme case mentioned above, this implies that for $\boldsymbol{E} \parallel \boldsymbol{a}$ only electrons with spin σ are excited and, vice versa, for $\boldsymbol{E} \parallel \boldsymbol{b}$ only electrons with spin $-\sigma$ are excited. When coming to evaluate on a quantitative level how photo-excited electron-spin can be controlled by light-polarization in realistic ultrafast-pumped AMs, it is clear that these symmetry considerations imply that a linearly polarized pump photon field can, in principle, couple differently to the two spin species.

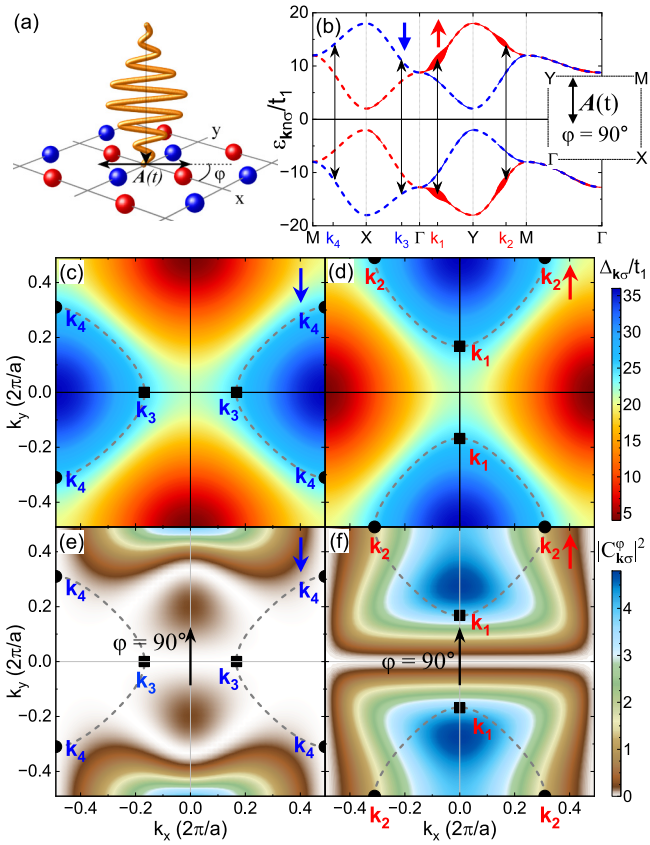

FIG. 1. (a) Sketch of the d-wave AM model and the vector potential $\boldsymbol{A}(t)$ of the pump pulse impinging on it. (b) Spin-up (red) and spin-down (blue) electronic bands. The thickness of the superimposed solid lines is proportional to the post-pump electron and hole photo-excited populations, for $A_0 = 0.2\frac{\hbar}{ea}$, $\omega_{\rm pu} = 25\frac{t_1}{\hbar}$, $\tau_{\rm pu} = 0.8\frac{\hbar}{t_1}$, and $\varphi = 90^\circ$. Momenta k_i, for $i = 1, \ldots, 4$, denote *resonant* $\boldsymbol{k}$-points. Only $k_{1,2}$ host non-negligible post-pump photo-excited populations because of the corresponding noticeable coupling to the pump pulse. (c)–(d) Band gap $\Delta_{\boldsymbol{k}\sigma}$ over the whole BZ for spin-down and spin-up bands, respectively. The dashed lines mark the positions of *resonant* $\boldsymbol{k}$-points. (e)–(f) Light-matter coupling strengths, $|C^{\varphi}_{\boldsymbol{k}\sigma}|^2$, over the whole BZ for spin-down and spin-up bands, respectively, and $\varphi = 90^\circ$.

II. d-WAVE AM MODEL HAMILTONIAN

To capture the photo-excitation behavior of an AM induced by a linearly polarized EM pulse, we first consider the simple realization of a d-wave AM introduced in Ref. [26]. The model takes the form of a 2D Lieb lattice shown in Fig. 1(a), where the antiparallel magnetic moments (blue and red dots) form two distinct sublattices related by fourfold rotation. The AM character emerges from the two sublattices having distinct local environments due to the presence of further non-magnetic sites [26]. A Kondo-type interaction couples frozen localized spins with itinerant electrons hopping only among the two magnetic sublattices, resulting in a spin-split band structure, see Fig. 1(b). For simplicity, we take a parametrization (see Appendix A) that comes with a clean gap between the AM bands at half filling, see Fig. 1(b). As expected, the spin-up, $\varepsilon_{\boldsymbol{k}n\uparrow}$, and spin-down, $\varepsilon_{\boldsymbol{k}n\downarrow}$, bands are related by a $\pi/2$ rotation in the $\boldsymbol{k}$ space [see Fig. 1(b)]. We indicate the valence (conduction) band by $n = 1(2)$. The spin-specific band gap, $\Delta_{\boldsymbol{k}\sigma} = \varepsilon_{\boldsymbol{k}2\sigma} - \varepsilon_{\boldsymbol{k}1\sigma}$, naturally exhibits the AM symmetry [see Figs. 1(c)–1(d)].

III. LIGHT PULSE IMPINGING ON A SOLID

To determine how an ultrafast EM pulse impacts the spin and charge distribution of photo-excited states in an AM, we start from the spin-conserving dipole-gauge Hamiltonian describing the interaction between a classical EM pulse in the dipole approximation and a solid-state lattice system [24,25,27]

$$\hat{H} = \sum_{\boldsymbol{k},\nu,\nu',\sigma} c^{\dagger}_{\boldsymbol{k}\nu\sigma} T_{\boldsymbol{k}+\frac{e}{\hbar}\boldsymbol{A}(t),\nu\nu'\sigma} c_{\boldsymbol{k}\nu'\sigma} + e\boldsymbol{E}(t) \cdot \sum_{\boldsymbol{k},\nu,\nu',\sigma} c^{\dagger}_{\boldsymbol{k}\nu\sigma} \boldsymbol{D}_{\boldsymbol{k}+\frac{e}{\hbar}\boldsymbol{A}(t),\nu\nu'\sigma} c_{\boldsymbol{k}\nu'\sigma}, \quad (1)$$

where $\boldsymbol{k}$ is the crystal momentum that is summed over the Brillouin zone (BZ), σ is the electronic spin, ν and ν' are sets of quantum numbers identifying orthogonal localized electronic states (e.g., the maximally localized Wannier states), $c_{\boldsymbol{k}\nu\sigma}$ ($c^{\dagger}_{\boldsymbol{k}\nu\sigma}$) is the annihilation (creation) operator of an electron in the state with quantum numbers $(\boldsymbol{k}, \nu, \sigma)$, $\boldsymbol{A}(t)$ is the vector potential and $\boldsymbol{E}(t) = -\partial_t \boldsymbol{A}(t)$ is the electric field of the impinging pulse. $T_{\boldsymbol{k}\nu\nu'\sigma}$ is the matrix element of the first-quantization (single-particle) equilibrium Hamiltonian and $\boldsymbol{D}_{\boldsymbol{k}\nu\nu'\sigma}$ is the matrix element of the local dipole in the reciprocal space.

IV. MECHANISM FOR POLARIZATION CONTROL OF POST-PUMP ELECTRON-SPIN DISTRIBUTION

Before presenting the calculated post-pump, nonequilibrium electron-spin distribution, we first elucidate the mechanism by which the polarization of the light pulse can control and switch the spin orientation of the excited electrons, a property that sets AMs apart from conventional FMs and AFMs. We consider a pump-pulse with a polarization in the lattice plane parametrized by the angle φ formed with the x axis, as indicated in Fig. 1(a). The cross-section for photoexcitation is large when the spin-specific band gap $\Delta_{\boldsymbol{k}\sigma}$ is in resonance with the pump-pulse frequency $\omega_{\rm pu}$. The resonant momenta are indicated by dashed lines in Figs. 1(c)–1(f) and include, for instance, momenta $\boldsymbol{k}_{1-4}$ indicated in Fig. 1(b). Here $\boldsymbol{k}_{1,2}$ correspond to resonances of spin-up electrons, and $\boldsymbol{k}_{3,4}$ to spin-down ones. It is important to note that due to the altermagnetic symmetry, $\boldsymbol{k}_{1,2}$ are related to $\boldsymbol{k}_{3,4}$ by a $\pi/2$ rotation. The light-matter coupling strength $C^{\varphi}_{\boldsymbol{k}\sigma}$ determines how strongly these states couple to the light field. In an AM, this essential ingredient depends in a nontrivial manner on the spin σ of the electronic states involved and the polarization φ of the light pulse. In the following, we will determine the expression of $C^{\varphi}_{\boldsymbol{k}\sigma}$ and its dependence on light-pulse characteristics explicitly. The calculated light-matter coupling strength for the d-wave AM model is shown in Figs. 1(e) and 1(f) for $\varphi = 90^{\circ}$ [28]. For this polarization direction, one observes that although $\boldsymbol{k}_{3,4}$ are in resonance, these states only couple weakly to the light field so that the post-pump density of spin-down states is low [see Fig. 2(d)]. However, for the same polarization direction, $\boldsymbol{k}_{1,2}$ strongly couple to the light field [Fig. 1(f)] and host a large spin-up density after pumping [Fig. 2(b)]. Because of the altermagnetic symmetry, the rotation of the incoming light-pulse polarization by $\pi/2$ exchanges the role of spin-up and spin-down, see Fig. 2, giving rise to spin-switching.

V. DYNAMICAL PROJECTIVE OPERATORIAL APPROACH (DPOA)

To determine quantitatively the impact of the pump pulse on the electronic state of the system, we use the DPOA [23–25], which efficiently and effectively study out-of-equilibrium systems by projecting the time-dependent operators on their equilibrium counterparts, $c_{kn\sigma}(t) = \sum_{n'} P_{knn'\sigma}(t) c_{kn'\sigma}$, and moving the solution of the operatorial dynamics to the solution of the equations of motion of the dynamical projection matrices, $P_{knn'\sigma}(t)$ (see Appendix B).

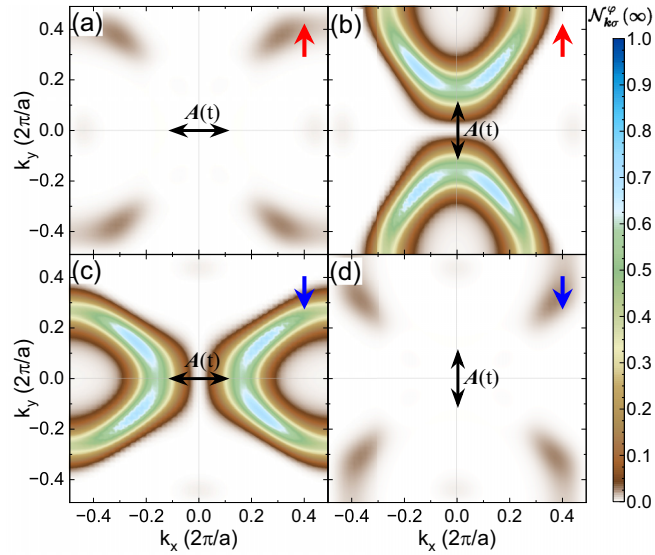

FIG. 2. The pump pulse polarization controls the spin of the photo-excited charge carriers: shown are the post-pump spin up/down electron populations, $\mathcal{N}^{\varphi}_{\boldsymbol{k}\sigma}(\infty)$, for pump pulse polarization $\varphi = 0/90^{\circ}$: (a), (b) spin-up, (c), (d) spin-down, (a), (c) $\varphi = 0^{\circ}$, and (b), (d) $\varphi = 90^{\circ}$.

In principle, this allows to compute any out-of-equilibrium response, such as time-resolved ARPES [24] and transient optical properties [25]. In particular, the electronic band populations can be obtained as $N_{kn\sigma}(t) = \langle c^{\dagger}_{kn\sigma}(t) c_{kn\sigma}(t)\rangle = \sum_{n'} P_{knn'\sigma}(t) f_{+}(\varepsilon_{kn'\sigma}) P^{\star}_{knn'\sigma}(t)$, where $f_{+}(\varepsilon)$ is the Fermi distribution function [24] (see Appendix B).

VI. RESULTING POST-PUMP ELECTRON-SPIN DISTRIBUTION

The pump pulse that we consider features a vector potential $\boldsymbol{A}(t) = A_0 e^{-(4\ln 2)t^2/\tau^2_{\rm pu}} \sin(\omega_{\rm pu} t)\hat{\boldsymbol{A}}$, where A_0 is its amplitude, $\tau_{\rm pu}$ is the FWHM of its Gaussian envelope centered at time $t = 0$, and $\omega_{\rm pu}$ is its central frequency. The electronic excited population, which is the positive excess post-pump electronic population with respect to the thermal equilibrium one summed over all bands, is denoted by $\mathcal{N}^{\varphi}_{\boldsymbol{k}\sigma}(\infty)$. Given that the main excitation processes in the model are due to one-photon resonances, the dimensionless light-matter coupling is determined from the off-diagonal element of the *velocity* (first-order) term in the Peierls expansion: $C^{\varphi}_{\boldsymbol{k}\sigma} = \frac{1}{t_1 a}\sum_{\nu\nu'} \Omega^{\dagger}_{\boldsymbol{k}1\nu'\sigma}(\partial_{k_A} T_{\mathbf{k}\nu'\nu\sigma})\Omega_{\boldsymbol{k}\nu 2\sigma}$ (see Appendix B). $|C^{\varphi}_{\boldsymbol{k}\sigma}|^2$ exhibits the same symmetry of $\varepsilon_{kn\sigma}$ and $\Delta_{k\sigma}$ under rotation of the polarization. As indicated above, for fixed polarization, $|C^{\varphi}_{\boldsymbol{k}\sigma}|^2$ is instead very different between spin-up and spin-down [see Figs. 1(e)–1(f)].

The post-pump electron photo-excited populations, $\mathcal{N}^{\varphi}_{\boldsymbol{k}\sigma}(\infty)$, of the d-wave AM model for the four relevant cases obtained by crossing the values of spin σ (up and down) and polarization φ (0° and 90°) are shown in Fig. 2. The noticeable difference in the coupling strength $|C^{\varphi}_{\boldsymbol{k}\sigma}|^2$ between spin-up and spin-down for the chosen pump pulse frequency and polarization ($\varphi = 90^{\circ}$), that is along the dashed lines of Figs. 1(e) and 1(f), leads to the huge difference between the

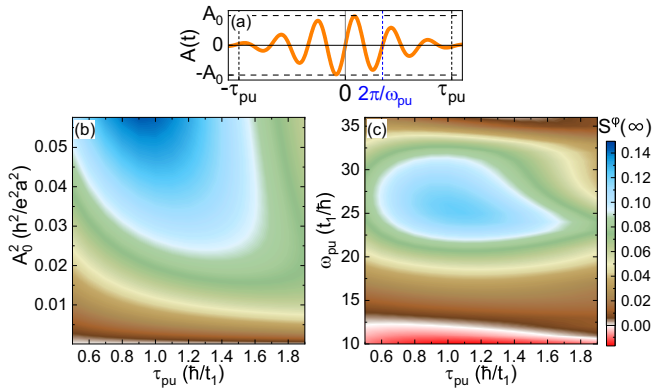

FIG. 3. (a) Characteristics of the vector potential of the pump pulse. (b)–(c) Post-pump electron photo-excited magnetization per unit cell, $S^{\varphi}(\infty)$, as a function of the FWHM, $\tau_{\rm pu}$, and (b) the square of the pump pulse amplitude, A_0^2, (c) the pump pulse frequency, $\omega_{\rm pu}$, for $\varphi = 90^{\circ}$ and the same parameter values of Fig. 1.

values of $\mathcal{N}^{\varphi}_{\boldsymbol{k}\uparrow}(\infty)$ and $\mathcal{N}^{\varphi}_{\boldsymbol{k}\downarrow}(\infty)$ in Figs. 2(b) and 2(d), and determines the regions in $\boldsymbol{k}$ space where one can find the higher values of $\mathcal{N}^{\varphi}_{\boldsymbol{k}\uparrow}(\infty)$: the momentum and spin selectivity by polarization is demonstrated. The symmetry of $\mathcal{N}^{\varphi}_{\boldsymbol{k}\sigma}(\infty)$ relates Figs. 2(a) and 2(c), to Figs. 2(b) and 2(d).

Having established that the pump pulse frequency, ω_{pu}, selects the *resonant* momentum region, and the pump pulse polarization, φ, is very effective in selecting the spin, we turn to the effects of the pulse's amplitude, A_0, and duration, measured through the FWHM, $\tau_{\rm pu}$, of its Gaussian envelope [see Fig. 3(a)]. In Figs. 3(b) and 3(c), we report the post-pump electron photo-excited magnetization per unit cell, $S^{\varphi}(\infty) = \frac{a^2}{4\pi^2}\int_{BZ}[\mathcal{N}^{\varphi}_{\boldsymbol{k}\uparrow}(\infty) - \mathcal{N}^{\varphi}_{\boldsymbol{k}\downarrow}(\infty)]d\boldsymbol{k}$, to discuss its dependence on pump pulse FWHM, amplitude, and frequency at fixed polarization ($\varphi = 90^{\circ}$).

Within the overall time span of the pump pulse, the electron photo-excited populations at (and close to) *resonant* $\boldsymbol{k}$-points undergo Rabi-like oscillations with a Rabi frequency, $\omega^{\varphi}_{R,k\sigma}$, which is proportional to $|C^{\varphi}_{k\sigma}|A_0$ [23,29]. Accordingly, the post-pump electron photo-excited populations, $\mathcal{N}^{\varphi}_{k\sigma}(\infty)$, is roughly proportional to $\sin^2(\omega^{\varphi}_{R,k\sigma}\tau_{\rm pu}/2)$, which can be approximated to $(\omega^{\varphi}_{R,k\sigma}\tau_{\rm pu}/2)^2$ for small enough pump pulse amplitudes and durations [29]. This explains why, in Fig. 3(b), $S^{\varphi}(\infty)$ increases monotonically with the pump pulse FWHM, $\tau_{\rm pu}$, only at small enough amplitudes, A_0, while it has a re-entrant behavior on continuously increasing $\tau_{\rm pu}$ for large enough values of A_0.

On varying the pump pulse frequency, ω_{pu}, instead, we change the loci of *resonant* $\boldsymbol{k}$-points within the BZ and, accordingly, we also explore the landscape of light-matter coupling strengths, $|C^{\varphi}_{k\sigma}|^2$ [compare to Figs. 1(c)–1(f)]. At the largest frequencies, in Fig. 3(c), the region of *resonant* $\boldsymbol{k}$-points is so small [see Figs. 1(c)–1(d)] that the reentrant behavior of $S^{\varphi}(\infty)$ on increasing $\tau_{\rm pu}$ is very difficult to resolve on the 2D map, while it is clearly visible for all other high and intermediate values of the frequency. For smaller and smaller values of the frequency, we observe an interesting new effect: the *number* of *resonant* $\boldsymbol{k}$-points with significant values of the coupling strength becomes more and more comparable

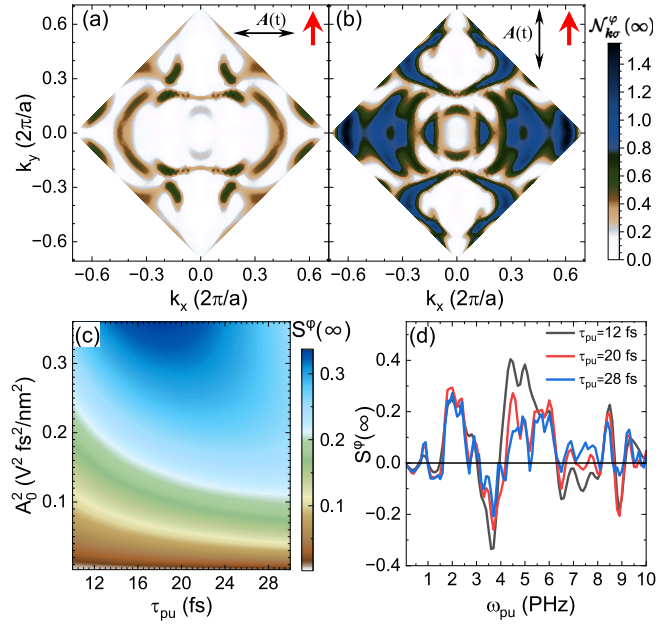

FIG. 4. Post-pump electron photo-excited populations, $\mathcal{N}^{\varphi}_{k\sigma}(\infty)$, for the bilayer RuO_2 for (a) $\varphi = 0^{\circ}$ and (b) $\varphi = 90^{\circ}$. The used pump pulse parameters are $A_0 = 2$ V fs/nm, $\omega_{\rm pu} = 2$ PHz, and $\tau_{\rm pu} = 12$ fs. The temperature is fixed at about 290 K (i.e., 25 meV). (c) Post-pump electron photo-excited magnetization per unit cell, $S^{\varphi}(\infty)$, for $\varphi = 90^{\circ}$ as a function of (c) the FWHM, $\tau_{\rm pu}$, and the square of the pump pulse amplitude, A_0^2, with $\omega_{\rm pu} = 2$ PHz and (d) the pump pulse frequency, $\omega_{\rm pu}$, and for $\tau_{\rm pu} = 12$, 20, and 28 fs with $A_0 = 2$ V fs/nm.

between the two spin orientations [compare to Figs. 1(c)–1(f)] up to an overtaking that reflects in an inversion of the sign of $S^{\varphi}(\infty)$ for $\omega_{\rm pu} \lesssim 10\frac{t_1}{\hbar}$ [the reddish area in Fig. 3(c)]. On increasing $\tau_{\rm pu}$ in this region of pump pulse frequencies, ω_{pu}, given the strong spin dependence of the Rabi frequency, $\omega^{\varphi}_{R,k\sigma}$, we scan values of $\mathcal{N}^{\varphi}_{k\sigma}(\infty)$ that again tend to compensate between the spin orientations over the whole BZ and increase the value of $S^{\varphi}(\infty)$ up to reestablishing its positivity.

VII. PUMPED ALTERMAGNETIC BILAYER

To demonstrate this phenomenology and the related effects also on the *ab initio* electronic structure of materials, with all their complexities in terms of band structure and number of active degrees of freedom, we performed a similar analysis on a prototype AM material—a RuO_2 bilayer (see Appendix C). While experiment evidences that bulk RuO_2 is not magnetic [30–33], altermagnetism can be stabilized in thin films [34,35]. In real materials, charge excitations decay because of electron-phonon scattering, spontaneous emission, etc. However, the time-scales of such processes are usually of the order of hundreds of femtoseconds [21,23,36,37], while the ultrafast pumping that we consider here occurs over a time-scale of tens of femtoseconds. Accordingly, the post-pump photo-excitations are computed well before such decay mechanisms become relevant. In Figs. 4(a) and 4(b), the post-pump electron photo-excited populations, $\mathcal{N}^{\varphi}_{k\sigma}(\infty)$, for $\varphi = 0^{\circ}$ and $\varphi = 90^{\circ}$, respectively, clearly show that through this protocol–varying the pump pulse polarization–, it is pos-

sible to excite different spin polarizations selectively both in specific regions of the BZ and overall in the system. This is further confirmed by looking at the post-pump electron photo-excited magnetization per unit cell, $S^{\varphi}(\infty)$, as a function of the pump pulse characteristics. In Fig. 4(c), despite the much larger complexity of the system under analysis, we recover the same qualitative behavior we have found for the d-wave AM model [compare to Fig. 3(b)] confirming the robustness of the phenomenology.

In Fig. 4(d), we see that $S^{\varphi}(\infty)$ can be easily tuned in absolute value and even in sign, on varying both the pump pulse frequency, ω_{pu}, and the FWHM, τ_{pu}, of the pump pulse. The complexity of *real* materials calls for different regions of the BZ for each spin orientation to become active at the same time, in terms of being single or multiphoton *resonant* and more or less coupled to the applied EM pump pulse. It is worth noting that, in *real* materials, we can have multiphoton resonances, and not necessarily just single-photon ones, and the former can become even dominant with respect to the latter [23].

The complexity of *real* materials does not hinder the phenomenology, which we proved to be very robust even in this case. Actually, such complexity allows for greater tunability and switchability, the possibility of designing and engineering altermagnetic materials for specific needs, and paves the way for an effective ultrafast optical control of AMs, with all possible future potential technological applications.

VIII. CONCLUSIONS AND PERSPECTIVES

The phenomenology and the effects discovered and demonstrated can be used (i) to identify altermagnetic materials via pump-probe Kerr and Faraday spectroscopies and/or spin- and time-resolved ARPES, (ii) to probe the spin polarization of the band structure of AMs in energy and momentum space, (iii) to generate photo-excited holes and electrons with a specific spin orientation that could be used to obtain bias-induced spin-polarized currents, and (iv) to devise an optical switch of the net spin polarization of photo-excited holes and electrons by tuning the pump pulse characteristics.

In parallel to our theoretical work, in recent magneto-optical measurements on RuO_2 films, the connection between the linear polarization of an impulsive pump pulse and the sign and magnitude of the optically excited electronic spin polarization has been demonstrated experimentally by Weber *et al.* [38]. The instantaneous optical excitation cross section is determined from Fermi's golden rule and subsequently the post-pump scattering dynamics of excitations is analyzed [39]. Here, instead, we determine the complete nonlinear response of the system to a time-dependent pump pulse, taking into account all single and multiphoton processes and the consequent Rabi-like oscillatory behaviors. In particular we have considered a Gaussian modulated sinusoidal pump pulse that allows one to exploit resonances and explore the full complexity of the BZ landscape in AMs. Accordingly, we have determined how the features of the pump pulse (polarization, frequency, amplitude, and duration) quantitatively affect the excitation of photo-induced charge carriers (their density, spin, and momentum).

ACKNOWLEDGMENTS

A.E. and A.A. acknowledge financial support from Ministero dell'Università (MUR) through the PNRR MUR Project No. PE0000023-NQSTI-TOPQIN. J.v.d.B. and O.J. acknowledge financial support from the Deutsche Forschungsgemeinschaft (DFG, German Research Foundation) through the Sonderforschungsbereich SFB 1143, Grant No. YE 232/2-1, and under Germany's Excellence Strategy through the Würzburg-Dresden Cluster of Excellence on Complexity and Topology in Quantum Matter– *ct.qmat* (EXC 2147, Project-IDs 390858490 and 392019).

DATA AVAILABILITY

The data that support the findings of this article are openly available [28].

APPENDIX A: THE d-WAVE AM MODEL

In the d-wave AM model [26], the Hamiltonian is parameterized by the Kondo interaction strength, J, the staggered magnetization vector, $\boldsymbol{N}$, a nearest-neighbor hopping, t_1, and anisotropic next-nearest-neighbor hoppings, t_{2a} and t_{2b}, over two sublattices A and B. Then, its matrix elements read as [26]

$$\begin{aligned} T_{\boldsymbol{k}\nu\nu'\sigma} = & -4t_1 \cos\frac{k_x}{2}\cos\frac{k_y}{2}\tau^x_{\nu\nu'} \\ & - 2t_2(\cos k_x + \cos k_y)\tau^0_{\nu\nu'} \\ & - 2t_d(\cos k_x - \cos k_y)\tau^z_{\nu\nu'} + JN_z\sigma\tau^z_{\nu\nu'}, \end{aligned} \tag{A1}$$

where $\nu, \nu' \in \{A, B\}$, τ^0, τ^x, τ^y and τ^z are the Pauli matrices, and $\sigma = +\ (-)$ corresponds to the spin-up (down). We set $N_z = \boldsymbol{N}\cdot\hat{z} = 1.25\frac{4t_d}{J}$, which is the staggered magnetization in the z direction. Moreover, we set $t_2 = \frac{t_{2a}+t_{2b}}{2} = 0.5t_1$, and $t_d = \frac{t_{2a}-t_{2b}}{2} = 2t_1$. In this model, $\boldsymbol{D}_{\boldsymbol{k}\nu\nu'\sigma} = 0$.

APPENDIX B: DYNAMICAL PROJECTIVE OPERATORIAL APPROACH (DPOA)

In principle, for a general time-dependent Hamiltonian $\mathcal{H}(t)$, it is always possible to find some sets of operators, $\mathcal{C}_\alpha$, that display a closed hierarchy of equations of motion: $\mathrm{i}\hbar\partial_t\mathcal{C}_\alpha(t) = [\mathcal{C}_\alpha(t), \mathcal{H}(t)] = \Xi_\alpha(t)\cdot\mathcal{C}_\alpha(t)$, where $\cdot$ is the matrix product in the space of the operators belonging to a specific set α, while $\Xi_\alpha(t)$ is known as the time-dependent *energy matrix* [24,40]. The DPOA [23–25] exploits this occurrence to efficiently and effectively study out-of-equilibrium systems by projecting the time-dependent operators on their equilibrium counterparts ($\mathcal{C}_\alpha(t) = P_\alpha(t)\cdot\mathcal{C}_\alpha$) and moving the solution of the operatorial dynamics to the solution of the equations of motion of the dynamical projection matrices $P_\alpha(t)$: $\mathrm{i}\hbar\partial_t P_\alpha(t) = \Xi_\alpha(t)P_\alpha(t)$. For a quadratic Hamiltonian of a solid-state lattice system, the operators $\mathcal{C}$ reduce to the electronic annihilation operators.

Usually, it is convenient to work in a basis that diagonalizes the equilibrium Hamiltonian: $T_{\boldsymbol{k}\nu\nu'\sigma}$ in Eq. (1). The transformation to such a basis, which we denote by the index n, is performed by a unitary matrix, $\Omega_{\boldsymbol{k}\nu n\sigma}$. The electronic annihilation operator in this basis reads as $c_{\boldsymbol{k}n\sigma}(t)$. The corre-

sponding eigenvalues are denoted by $\varepsilon_{\boldsymbol{k}n\sigma}$, and are the bands of the system. One fundamental ingredient in the DPOA framework is the use of the so-called Peierls expansion, which is a Taylor expansion for computing very efficiently $T_{\boldsymbol{k}+\frac{e}{\hbar}\boldsymbol{A}(t)\nu\nu'\sigma}$ and $\boldsymbol{D}_{\boldsymbol{k}+\frac{e}{\hbar}\boldsymbol{A}(t)\nu\nu'\sigma}$ in Eq. (1) [24]: $\chi_{\boldsymbol{k}+\frac{e}{\hbar}\boldsymbol{A}(t)}(t) = \sum_{m=0}^{\infty}\frac{1}{m!}(\frac{e}{\hbar}A(t))^m(\partial_{k_A})^m\chi_{\boldsymbol{k}}$, where $k_A = \boldsymbol{k}\cdot\hat{\boldsymbol{A}}$ and $\hat{\boldsymbol{A}}$ is the polarization of $\boldsymbol{A}(t) = A(t)\hat{\boldsymbol{A}}$.

APPENDIX C: DETAILS OF THE RuO_2 BILAYER

While there is a mounting experimental evidence that bulk RuO_2 is not magnetic [30–33], altermagnetism can be stabilized in thin films [34,35]. Here, we consider a free-standing bilayer of RuO_2, which we use as a prototype system with an effective d-wave AM model that mimics the complexity of *real* materials. To construct an altermagnetic bilayer, we start from the bulk crystal structure and make a slab with two formula units oriented along the c-axis of the bulk system. Opposite-spin Ru ions are related by fourfold roto-inversion symmetry, and the system can be represented as a $\sqrt{2}\times\sqrt{2}\times 1$ supercell described within the space group $Cmm2$ (35) with $a = 6.35$ Å. For this structure, we perform density-functional calculations in GGA+U [41,42], as implemented in the Wien2k code [43]. We use the full localized limit for the double counting correction and parameters $U = 1.52$ eV and $J = 0.4$ eV. For the BZ integrations, we use a k-point mesh having 2000 k-points in the irreducible BZ, along with a tetrahedron method. The calculation of the post-pump excitations exploits a Wannier model based on Ru $4d$ and O $2p$ orbitals, which was obtained with the Wannier90 code [44]. The model successfully reproduces the DFT band structure in the energy range $[-7$ eV, 3 eV$]$ around the Fermi energy.

[1] L. Šmejkal, R. González-Hernández, T. Jungwirth, and J. Sinova, Crystal time-reversal symmetry breaking and spontaneous Hall effect in collinear antiferromagnets, Sci. Adv. **6**, eaaz8809 (2020).

[2] L. Šmejkal, J. Sinova, and T. Jungwirth, Beyond conventional ferromagnetism and antiferromagnetism: A phase with nonrelativistic spin and crystal rotation symmetry, Phys. Rev. X **12**, 031042 (2022).

[3] L. Šmejkal, J. Sinova, and T. Jungwirth, Emerging research landscape of altermagnetism, Phys. Rev. X **12**, 040501 (2022).

[4] M. Naka, S. Hayami, H. Kusunose, Y. Yanagi, Y. Motome, and H. Seo, Spin current generation in organic antiferromagnets, Nat. Commun. **10**, 4305 (2019).

[5] L.-D. Yuan, Z. Wang, J.-W. Luo, E. I. Rashba, and A. Zunger, Giant momentum-dependent spin splitting in centrosymmetric low-z antiferromagnets, Phys. Rev. B **102**, 014422 (2020).

[6] M. Naka, Y. Motome, and H. Seo, Perovskite as a spin current generator, Phys. Rev. B **103**, 125114 (2021).

[7] Y. Guo, H. Liu, O. Janson, I. C. Fulga, J. van den Brink, and J. I. Facio, Spin-split collinear antiferromagnets: A large-scale *ab-initio* study, Mater. Today Phys. **32**, 100991 (2023).

[8] P. A. McClarty and J. G. Rau, Landau theory of altermagnetism, Phys. Rev. Lett. **132**, 176702 (2024).

[9] T. Sato, S. Haddad, I. C. Fulga, F. F. Assaad, and J. van den Brink, Altermagnetic anomalous Hall effect emerging from electronic correlations, Phys. Rev. Lett. **133**, 086503 (2024).

[10] M. Trama, I. Gaiardoni, C. Guarcello, J. I. Facio, A. Maiellaro, F. Romeo, R. Citro, and J. van den Brink, Nonlinear anomalous Edelstein response at altermagnetic interfaces, arXiv:2410.18036.

[11] M. Hu, O. Janson, C. Felser, P. McClarty, J. van den Brink, and M. G. Vergniory, Spin Hall and Edelstein effects in novel chiral noncollinear altermagnets, arXiv:2410.17993.

[12] P. M. Cônsoli, M. Fornoville, and M. Vojta, Fluctuation-induced ferrimagnetism in sublattice-imbalanced antiferromagnets with application to $SrCu_2(BO_3)_2$ under pressure, Phys. Rev. B **104**, 064422 (2021).

[13] T. Aoyama and K. Ohgushi, Piezomagnetic properties in altermagnetic MnTe, Phys. Rev. Mater. **8**, L041402 (2024).

[14] K. V. Yershov, V. P. Kravchuk, M. Daghofer, and J. van den Brink, Fluctuation-induced piezomagnetism in local moment altermagnets, Phys. Rev. B **110**, 144421 (2024).

[15] K. V. Yershov, O. Gomonay, J. Sinova, J. van den Brink, and V. P. Kravchuk, Curvature-induced magnetization of altermagnetic films, Phys. Rev. Lett. **134**, 116701 (2025).

[16] M. Vila, V. Sunko, and J. E. Moore, Orbital-spin locking and its optical signatures in altermagnets, arXiv:2410.23513.

[17] T. Brabec and F. Krausz, Intense few-cycle laser fields: Frontiers of nonlinear optics, Rev. Mod. Phys. **72**, 545 (2000).

[18] F. Schmitt, P. S. Kirchmann, U. Bovensiepen, R. G. Moore, L. Rettig, M. Krenz, J.-H. Chu, N. Ru, L. Perfetti, D. Lu *et al.*, Transient electronic structure and melting of a charge density wave in $TbTe_3$, Science **321**, 1649 (2008).

[19] F. Krausz and M. Ivanov, Attosecond physics, Rev. Mod. Phys. **81**, 163 (2009).

[20] F. Krausz and M. I. Stockman, Attosecond metrology: From electron capture to future signal processing, Nat. Photonics **8**, 205 (2014).

[21] M. Zürch, H.-T. Chang, L. J. Borja, P. M. Kraus, S. K. Cushing, A. Gandman, C. J. Kaplan, M. H. Oh, J. S. Prell, D. Prendergast, C. D. Pemmaraju, D. M. Neumark, and S. R. Leone, Direct and simultaneous observation of ultrafast electron and hole dynamics in germanium, Nat. Commun. **8**, 15734 (2017).

[22] R. Borrego-Varillas, M. Lucchini, and M. Nisoli, Attosecond spectroscopy for the investigation of ultrafast dynamics in atomic, molecular and solid-state physics, Rep. Prog. Phys. **85**, 066401 (2022).

[23] G. Inzani, L. Adamska, A. Eskandari-asl, N. D. Palo, G. L. Dolso, B. Moio, L. J. D'Onofrio, A. Lamperti, A. Molle, R. Borrego-Varillas, M. Nisoli, S. Pittalis, C. A. Rozzi, A. Avella, and M. Lucchini, Field-driven attosecond charge dynamics in germanium, Nat. Photonics **17**, 1059 (2023).

[24] A. Eskandari-asl and A. Avella, Time-resolved ARPES signal in pumped semiconductors within the dynamical projective operatorial approach, Phys. Rev. B **110**, 094309 (2024).

[25] A. Eskandari-asl and A. Avella, Generalized linear response theory for pumped systems and its application to transient optical properties, Phys. Rev. A **110**, 043520 (2024).

[26] D. S. Antonenko, R. M. Fernandes, and J. W. F. Venderbos, Mirror Chern bands and Weyl nodal loops in altermagnets, Phys. Rev. Lett. **134**, 096703 (2025).

[27] M. Schüler, J. A. Marks, Y. Murakami, C. Jia, and T. P. Devereaux, Gauge invariance of light-matter interactions in first-principle tight-binding models, Phys. Rev. B **103**, 155409 (2021).

[28] A. Eskandari-asl, J. I. Facio, O. Janson, A. Avella, and J. van den Brink, Data set "Controlling photoexcited electron spin by light polarization in ultrafast-pumped altermagnets", Version v1, Zenodo (2025), https://doi.org/10.5281/zenodo.15446591.

[29] A. Eskandari-asl and A. Avella, Dynamical projective operatorial approach (DPOA) for pump-probe setups in the ultrafast regime, in *Advances in Ultrafast Condensed Phase Physics IV, Strasbourg, France*, SPIE Proc. No. 12992 (SPIE, Bellingham, Washington, 2024), pp. 69–73.

[30] M. Hiraishi, H. Okabe, A. Koda, R. Kadono, T. Muroi, D. Hirai, and Z. Hiroi, Nonmagnetic ground state in RuO_2 revealed by muon spin rotation, Phys. Rev. Lett. **132**, 166702 (2024).

[31] J. Liu, J. Zhan, T. Li, J. Liu, S. Cheng, Y. Shi, L. Deng, M. Zhang, C. Li, J. Ding, Q. Jiang, M. Ye, Z. Liu, Z. Jiang, S. Wang, Q. Li, Y. Xie, Y. Wang, S. Qiao, J. Wen *et al.*, Absence of altermagnetic spin splitting character in rutile oxide RuO_2, Phys. Rev. Lett. **133**, 176401 (2024).

[32] L. Kiefer, F. Wirth, A. Bertin, P. Becker, L. Bohatý, K. Schmalzl, A. Stunault, J. A. Rodríguez-Velamazán, O. Fabelo, and M. Braden, Crystal structure and absence of magnetic order in single crystalline RuO_2, J. Phys. Condens. Matter **37**, 135801 (2025).

[33] M. Wenzel, E. Uykur, S. Rößler, M. Schmidt, O. Janson, A. Tiwari, M. Dressel, and A. A. Tsirlin, Fermi-liquid behavior of nonaltermagnetic RuO_2, Phys. Rev. B **111**, L041115 (2025).

[34] S. G. Jeong, I. H. Choi, S. Nair, L. Buiarelli, B. Pourbahari, J. Y. Oh, N. Bassim, D. Hirai, A. Seo, W. S. Choi, R. M. Fernandes, T. Birol, L. Zhao, J. S. Lee, and B. Jalan, Altermagnetic polar metallic phase in ultra-thin epitaxially-strained RuO_2 films, arXiv:2405.05838.

[35] A. Smolyanyuk, I. I. Mazin, L. Garcia-Gassull, and R. Valentí, Fragility of the magnetic order in the prototypical altermagnet RuO_2, Phys. Rev. B **109**, 134424 (2024).

[36] C. J. Kaplan, P. M. Kraus, A. D. Ross, M. Zürch, S. K. Cushing, M. F. Jager, H.-T. Chang, E. M. Gullikson, D. M. Neumark, and S. R. Leone, Femtosecond tracking of carrier relaxation in germanium with extreme ultraviolet transient reflectivity, Phys. Rev. B **97**, 205202 (2018).

[37] S. Marcinkevičius and J. S. Speck, Electron-phonon scattering in β-Ga_2O_3 studied by ultrafast transmission spectroscopy, Appl. Phys. Lett. **118**, 242107 (2021).

[38] M. Weber, S. Wust, L. Haag, A. Akashdeep, K. Leckron, C. Schmitt, R. Ramos, T. Kikkawa, E. Saitoh, M. Kläui, L. Šmejkal, J. Sinova, M. Aeschlimann, G. Jakob, B. Stadtmüller, and H. C. Schneider, All optical excitation of spin polarization in *d*-wave altermagnets, arXiv:2408.05187.

[39] M. Weber, K. Leckron, L. Haag, R. Jaeschke-Ubiergo, L. Šmejkal, J. Sinova, and H. C. Schneider, Ultrafast electron dynamics in altermagnetic materials, arXiv:2411.08160.

[40] A. Avella and F. Mancini, The composite operator method (com), in *Strongly Correlated Systems: Theoretical Methods* (Springer, Berlin, Heidelberg, 2011), pp. 103–141.

[41] J. P. Perdew, K. Burke, and M. Ernzerhof, Generalized gradient approximation made simple, Phys. Rev. Lett. **78**, 1396 (1997).

[42] V. I. Anisimov, I. V. Solovyev, M. A. Korotin, M. T. Czyżyk, and G. A. Sawatzky, Density-functional theory and NiO photoemission spectra, Phys. Rev. B **48**, 16929 (1993).

[43] P. Blaha, K. Schwarz, F. Tran, R. Laskowski, G. K. H. Madsen, and L. D. Marks, WIEN2k: An APW+lo program for calculating the properties of solids, J. Chem. Phys. **152**, 074101 (2020).

[44] G. Pizzi, V. Vitale, R. Arita, S. Blügel, F. Freimuth, G. Géranton, M. Gibertini, D. Gresch, C. Johnson, T. Koretsune, J. Ibañez-Azpiroz, H. Lee, J.-M. Lihm, D. Marchand, A. Marrazzo, Y. Mokrousov, J. I. Mustafa, Y. Nohara, Y. Nomura, L. Paulatto *et al.*, Wannier90 as a community code: New features and applications, J. Phys.: Condens. Matter **32**, 165902 (2020).